Fracture Mechanics of Concrete and Concrete Structures - Recent Advances in Fracture Mechanics of Concrete - B. H. Oh, et al.(eds)

The Lattice Discrete Particle Model (LDPM) for the Simulation of Uniaxial and Multiaxial Behavior of Concrete: Recent Results.

G. Cusatis & A. Mencarelli
Rensselaer Polytechnic Institute, Troy (NY), USA

D. Pelessone
ES3, Solana Beach (CA), USA

J.T. Baylot
Engineer Research and Development Center, Vicksburg (MS), USA

ABSTRACT: This paper presents recent results obtained by the Lattice Discrete Particle Model (LDPM) for the simulation of concrete and fiber reinforced concrete behavior. LDPM is a meso-scale model which has been recently formulated at Rensselaer Polytechnic Institute and extensively validated against experimental data. LDPM can accurately predict several phenomena characterizing concrete behavior, including failure under uniaxial, biaxial, and triaxial compression; material compaction under hydrostatic compression; and tensile fracturing.

1 THE LATTICE DISCRETE PARTICLE MODEL

Since the mid-1980s, many meso-scale models for concrete have appeared in the literature. The main advantage of these models over classic constitutive models for concrete is their ability to simulate material heterogeneity and its effect on damage evolution and fracture. Noteworthy examples of meso-scale models are the ones published in Roelfstra et al. (1985), Wittmann et al. (1988), Bažant et al. (1990), Schlangen & Van Mier (1992), Carol et al. (2001), Lilliu & Van Mier (2003), Cusatis et al. (2003a), Cusatis et al. (2003b), Cusatis et al. (2006a), Cusatis & Cedolin (2006b), Yip et al. (2006).

This paper presents and discusses recent results obtained at Rensselaer Polytechnic Institute by the Lattice Discrete Particle Model (LDPM). LDPM simulates concrete mesostructure by taking into account only the coarse aggregate pieces, typically with characteristic size greater than 5 mm. The mesostructure is constructed through the following steps. 1) The coarse aggregate pieces, whose shapes are assumed to be spherical, are introduced into the concrete volume by a try-and-reject random procedure. 2) Zero-radius aggregate pieces (nodes) are randomly distributed over the external surfaces. 3) A three-dimensional domain tessellation, based on the Delaunay tetrahedralization of the generated aggregate centers, creates a system of cells interacting through triangular facets, which can be represented in a two-dimensional sketch by straight line segments (Fig. 1). A vectorial constitutive law governing the behavior of the model is imposed at the centroid of the projection of each single facet (contact point) onto a plane orthogonal to the straight line connecting the particle centers (edges of the tetrahedralization). The projections are used instead of the facets themselves to ensure that the shear interaction between adjacent particles does not depend on the shear orientation. The straight lines connecting the contact points with the particle centers define the lattice system.

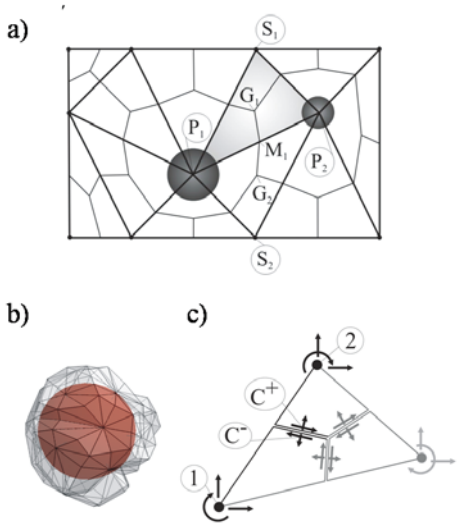

Figure 1: a) Meso-structure tessellation. b) Three-dimensional discrete particle. c) Definition of nodal degrees of freedom and contact facets in two-dimension.

Rigid body kinematics describes the displacement field along the lattice struts and the displacement jump, $[\![\mathbf{u}_C]\!]$, at the contact point. The strain vector is defined as the displacement jump at the contact point divided by the inter-particle distance, L. The components of the strain vector in a local system of reference, characterized by the unit vectors **n**, **l**, and **m**, are the normal and shear strains:

$$\varepsilon_N = \frac{\mathbf{n}^{\mathrm{T}}[\![\mathbf{u}_C]\!]}{L}; \quad \varepsilon_L = \frac{\mathbf{l}^{\mathrm{T}}[\![\mathbf{u}_C]\!]}{L}; \quad \varepsilon_M = \frac{\mathbf{m}^{\mathrm{T}}[\![\mathbf{u}_C]\!]}{L} \quad (1)$$

The unit vector **n** is orthogonal to the projected facet, and the unit vectors **l** and **m** are mutually orthogonal and lie in the projected facet.

The elastic behavior is described by assuming that the normal and shear stresses are proportional to the corresponding strains:

$$\sigma_N = E_N \varepsilon_N;\ \sigma_M = E_T \varepsilon_M;\ \sigma_L = E_T \varepsilon_L \quad (2)$$

where $E_N = E_0$, $E_T = \alpha E_0$, $E_0 =$ effective normal modulus, and $\alpha =$ shear-normal coupling parameter. E_0 and α are assumed to be material properties.

The tensile fracturing behavior ($\varepsilon_N > 0$) is formulated through a relationship between the *effective strain* and the *effective stress* (Cusatis et al. 2003a), defined as:

$$\varepsilon = \sqrt{\varepsilon_N^2 + \alpha(\varepsilon_M^2 + \varepsilon_L^2)}; \quad \sigma = \sqrt{\sigma_N^2 + \frac{(\sigma_M + \sigma_L)^2}{\alpha}} \quad (3)$$

By using the effective strain and the effective stress, the relationship between normal and shear stresses versus normal and shear strains can be calculated in a way similar to simple damage models(see derivation in Cusatis et al. (2003a)):

$$\sigma_N = \sigma \frac{\varepsilon_N}{\varepsilon}; \quad \sigma_M = \sigma \frac{\alpha \varepsilon_M}{\varepsilon}; \quad \sigma_L = \sigma \frac{\alpha \varepsilon_L}{\varepsilon} \quad (4)$$

The effective stress, σ, is incrementally elastic ($\dot{\sigma} = E_0 \dot{\varepsilon}$) and must satisfy the inequality $0 \leq \sigma \leq \sigma_{bt}(\varepsilon, \omega)$. The strain dependent boundary $\sigma_{bt}(\varepsilon, \omega)$ can be expressed as

$$\sigma_{bt} = \sigma_0(\omega) \exp\left[-H_0(\omega) \frac{\langle \varepsilon_{\max} - \varepsilon_0(\omega) \rangle}{\sigma_0(\omega)}\right] \quad (5)$$

in which the brackets $\langle \bullet \rangle$ are used in Macaulay sense: $\langle x \rangle = \max\{x, 0\}$.

The internal variable ω is defined as follows (Cusatis et al. 2003a):

$$\tan \omega = \frac{\varepsilon_N}{\sqrt{\alpha}\varepsilon_T} = \frac{\sigma_N \sqrt{\alpha}}{\sigma_T} \quad (6)$$

and it characterizes the coupling between normal and shear strains (or stresses). The σ_{bt} boundary evolves exponentially as a function of the maximum effective strain, which is a history-dependent variable defined as $\varepsilon_{\max} = \sqrt{\varepsilon_{N,\max}^2 + \alpha \varepsilon_{T,\max}^2}$, where $\varepsilon_{N,\max}(t) = \max_{\tau<t}[\varepsilon_N(\tau)]$ and $\varepsilon_{T,\max}(t) = \max_{\tau<t}[\varepsilon_T(\tau)]$ are the maximum normal and total shear strains, respectively, attained during the loading history (in absence of unloading $\varepsilon_{\max} \equiv \varepsilon$).

The function $\sigma_0(\omega)$ is the strength limit for the effective stress and is defined as follows:

$$\sigma_0(\omega) = \sigma_t \frac{-\sin(\omega) + \sqrt{\sin^2(\omega) + 4\alpha \cos^2(\omega)/r_{st}^2}}{2\alpha \cos^2(\omega)/r_{st}^2} \quad (7)$$

in which $r_{st} = \sigma_s/\sigma_t$ is the ratio between the shear strength (cohesion), σ_s, and the tensile strength, σ_t. In the stress space $\sigma_N - \sigma_T$, Equation 7 represents a parabola with its axis coincident with the σ_N-axis.

The exponential decay of the σ_{bt} boundary starts when the maximum effective strain reaches its elastic limit, $\varepsilon_0(\omega) = \sigma_0(\omega)/E_0$; and the decay rate is governed by the post-peak slope (softening modulus), which is assumed to be a power function of the internal variable ω:

$$H_0(\omega) = H_t \left(\frac{2\omega}{\pi}\right)^{n_t} \quad (8)$$

Equation 8 provides a smooth transition from softening behavior under pure tensile stress ($\omega = \pi/2$, $H_0(\omega) = H_t$) to perfectly plastic behavior under pure shear ($\omega = 0$, $H_0(\omega) = 0$). In order to preserve the correct energy dissipation during mesoscale damage localization (Bažant & Oh 1983), the softening modulus in pure tension is expressed as $H_t = 2E_0/(L_{cr}/L - 1)$, where G_t is the mesoscale fracture energy, $L_{cr} = 2E_0 G_t/\sigma_t^2$, and L is the length of the tetrahedron edge associated with the current facet.

For compressive loading ($\varepsilon_N < 0$), the normal stress is computed by imposing the inequality $-\sigma_{bc}(\varepsilon_D, \varepsilon_V) \leq \sigma_N \leq 0$, where σ_{bc} is a strain-dependent boundary depending on the volumetric strain, ε_V, and the deviatoric strain, ε_D. The volumetric strain is computed by considering the interaction of the four particles located at the vertexes of each Delaunay tetrahedron.

For a constant deviatoric strain to volumetric strain ratio, $r_{DV} = \varepsilon_D/\varepsilon_V$, the compressive boundary $\sigma_{bc}(r_{DV}, \varepsilon_V)$ is assumed to have an initial linear evolution (modeling pore collapse) followed by an exponential evolution (modeling compaction and rehardening). One can write the following:

$$\sigma_{bc} = \sigma_{c0} + \langle -\varepsilon_V - \varepsilon_{c0} \rangle H_c \quad (9)$$

for $-\varepsilon_V \leq \varepsilon_{c1}$ and

$$\sigma_{bc} = \sigma_{c1} \exp\left[(-\varepsilon_V - \varepsilon_{c1}) H_c/\sigma_{c1}\right] \quad (10)$$

otherwise; $\sigma_{c0} =$ yielding compressive stress, $\varepsilon_{c0} = \sigma_{c0}/E_0 =$ volumetric strain at the onset of pore collapse, $H_c =$ initial hardening modulus, $\varepsilon_{c1} = \lambda_{c0}\varepsilon_{c0} =$ volumetric strain at which rehardening begins, $\lambda_{c0} =$ material parameter governing the onset of rehardening, and $\sigma_{c1} = \sigma_{c0} + (\varepsilon_{c1} - \varepsilon_{c0})H_c$.

For increasing r_{DV}, the slope of the initial hardening modulus must tend to zero in order to simulate the

observed horizontal plateau featured by typical experimental data. This can be achieved by setting

$$H_c(r_{DV}) = \frac{H_{c0}}{1 + \kappa_{c2} \langle r_{DV} - \kappa_{c1} \rangle} \tag{11}$$

where $H_{c0} = \kappa_{c0} E_N$ and κ_{c0}, κ_{c1}, κ_{c2} are material parameters.

In the presence of compressive stresses, the shear strength increases due to frictional effects. This effect can be simulated effectively through classical incremental plasticity. Incremental shear stresses can be calculated as $\dot{\sigma}_M = E_T(\dot{\varepsilon}_M - \dot{\varepsilon}^p_M)$ and $\dot{\sigma}_L = E_T(\dot{\varepsilon}_L - \dot{\varepsilon}^p_L)$, where the plastic strain increments are assumed to obey the normality rule $\dot{\varepsilon}^p_M = \dot{\lambda} \partial\varphi / \partial\sigma_M$ and $\dot{\varepsilon}^p_L = \dot{\lambda} \partial\varphi / \partial\sigma_L$, where λ is the plastic multiplier.

The plastic potential can be expressed as $\varphi = \sqrt{\sigma^2_M + \sigma^2_L} - \sigma_{bs}(\sigma_N)$ in which the shear strength, σ_{bs}, is formulated with a nonlinear frictional law

$$\sigma_{bs} = \sigma_s + (\mu_0 - \mu_\infty)\sigma_{N0} - \mu_\infty \sigma_N - \\ -(\mu_0 - \mu_\infty)\sigma_{N0} \exp(\sigma_N / \sigma_{N0}) \tag{12}$$

where σ_s = cohesion, μ_0 and μ_∞ are the initial and final internal friction coefficients, respectively, and σ_{N0} = the normal stress at which the internal friction coefficient transitions from μ_0 to μ_∞. Finally, equations governing the shear stress evolution must be completed by the loading-unloading conditions $\varphi\dot{\lambda} \leq 0$ and $\dot{\lambda} \geq 0$.

Current LDPM formulation has been implemented into MARS, a multi-purpose computational code for the explicit dynamic simulation of structural performance (Pelessone 2009).

2 THREE-POINT BENDING TESTS

In this section LDPM is validated by simulating three-point bending (TPB) tests of notched specimens of three different sizes. Figure 2a shows the geometry of the medium size specimen. The geometric data of the specimens are reported in Table 1, where S and d are the specimen length and depth, and a is the notch depth. Damage evolution during TPB tests is characterized by the growth of a crack that initiates at the notch tip and propagates toward the opposite side of the specimen (Fig. 2b). Since fracture occurs in a very localized region, the numerical simulations were carried out by modeling only the central part of the specimens (in the vicinity of the notch) with LDPM and by using standard elastic finite elements in the zones where elastic behavior was expected. Coupling between LDPM and solid finite elements was obtained through a master-slave formulation (Cusatis et al. 2006a).

For the calibration of the material model parameters, the load displacement curve of the medium size specimen (Fig. 2c), the compressive strength, and the estimated pressure-volume curve under hydrostatic compression were used. After the completion of the calibration step, the simulations of the small size specimen and large size specimen were carried out for validation purposes without permitting further adjustment of the material model parameters. The agreement between the numerical simulations and the experimental data is excellent overall. This proves that LDPM can accurately simulate fracture propagation in concrete and that it can predict the dependence of structural strength on the structural size (size-effect).

Table 1: Geometric data for three-point bending tests.

Specimen	S [mm]	d [mm]	a [mm]
Small	840	100	50
Medium	1188	200	100
Large	1455	300	150

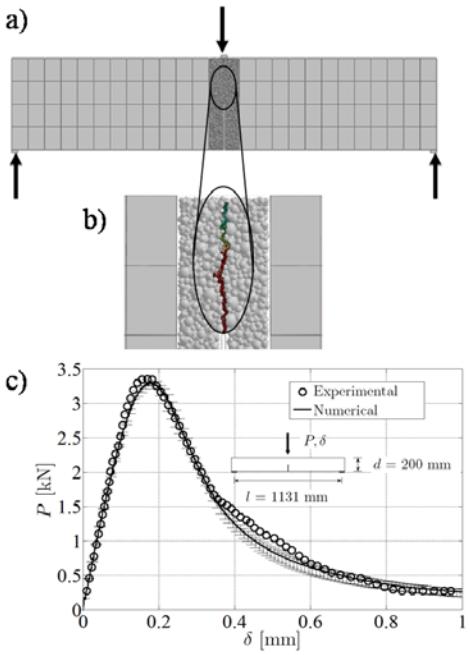

Figure 2: Three-point bending tests.

3 UNIAXIAL COMPRESSION

In this section calibration and validation of LDPM is presented with reference to uniaxial compression strength tests performed on prismatic specimens with a cross section of 100×100 mm^2 and three different heights: 50 mm, 100 mm, and 200 mm.

In the experiments (Van Mier et al. 1997), the load was applied under displacement control by a loading device which prevented rotation of the loading platens. The tests were performed in two ways: with untreated loading platens (high friction) and with platens covered by friction-reducing material (low friction). To simulate these two conditions, a simplified frictional boundary was used as proposed in Cusatis et al. (2003b).

The calibration of the LDPM parameters was obtained by fitting the stress-strain curve relevant to

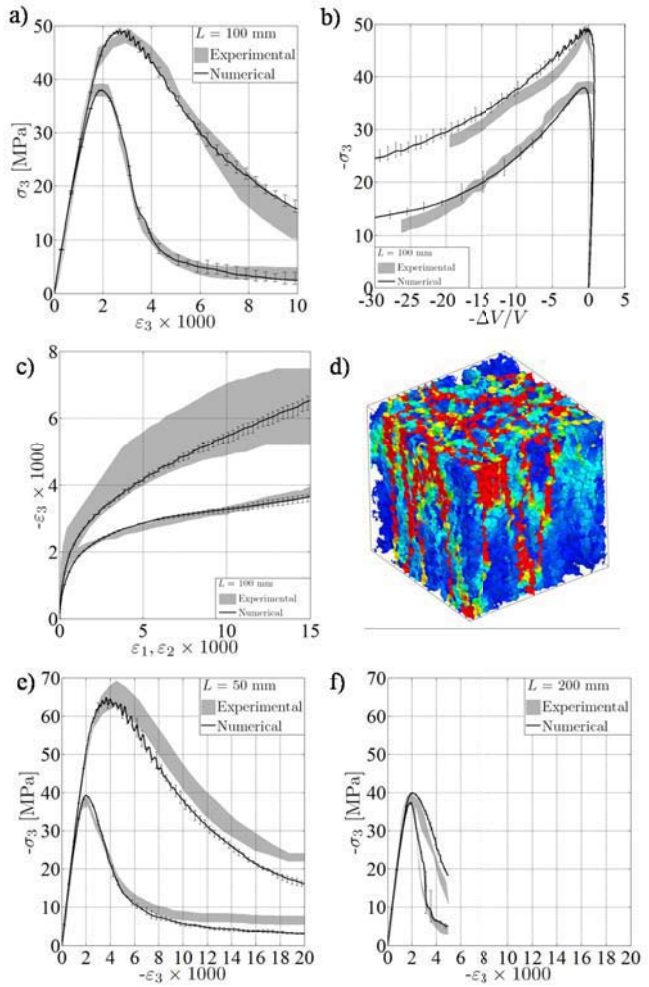

Figure 3: Uniaxial compression test results.

cubic specimens with low friction at specimen ends (Fig. 3a). The calibration procedure also required the simulation of a hydrostatic compression test, a splitting (Brazilian) test, and a three-point bending (TPB) test . The relevant experimental data, not available in Van Mier et al. (1997), were estimated on the basis of available literature on similar concretes (Bažant & Planas 1998). In addition, fitting of the high friction stress-strain curve for the cubic specimens (Fig. 3a) allowed for the calibration of the friction parameters. In Figures 3a, b, and c, the experimental curves relevant to the cubic specimens are compared with the average of three numerical results obtained by running the same tests with specimens featuring different generated mesostructures. Error bars show the scatter of the numerical solutions. Figure 3d shows a typical failure mode for low-friction conditions.

After calibrating the model, validation simulations were performed without further adjustment of the parameters. This was obtained by simulating uniaxial compression tests of prisms with length L = 50 mm and 200 mm. Figure 3f shows the results relevant to L = 200 mm. The numerical simulations predicted very accurately both peak stress and post-peak behavior of the stress-strain curves for both low platen friction and high platen friction. Figure 3e shows comparisons between experimental data and numerical results relevant to L = 50 mm. Overall the agreement is excellent and only the peak stress of the stress-strain curve for the low-friction case is predicted with less (but still acceptable) accuracy with respect to the other cases.

It must be noted here that the macroscopic strain-softening behavior captured by the model is the effect of tensile fracturing and shearing in the mesostructure rather than a phenomenological formulation of compressive softening, as typically done in continuum-based models.

4 BIAXIAL COMPRESSION

In this section the numerical simulation of biaxial tests is discussed with reference to the experimental data reported in Kupfer et al. (1969). In the experimental campaign, concrete panels (200 mm × 200 mm × 50 mm) were subjected to biaxial compression, biaxial compression-tension, and biaxial tension. The load was applied by means of brush-bearing platens to reduce the effect of friction.

The adopted loading paths were proportional in the space of the in-plane principal stresses σ_1 and σ_3, i.e. $k = \sigma_3/\sigma_1 =$ constant. Figure 4a shows the experimental (circles) and numerical (solid line) failure envelope, which is constructed from the peak stresses for various values of k normalized by the uniaxial

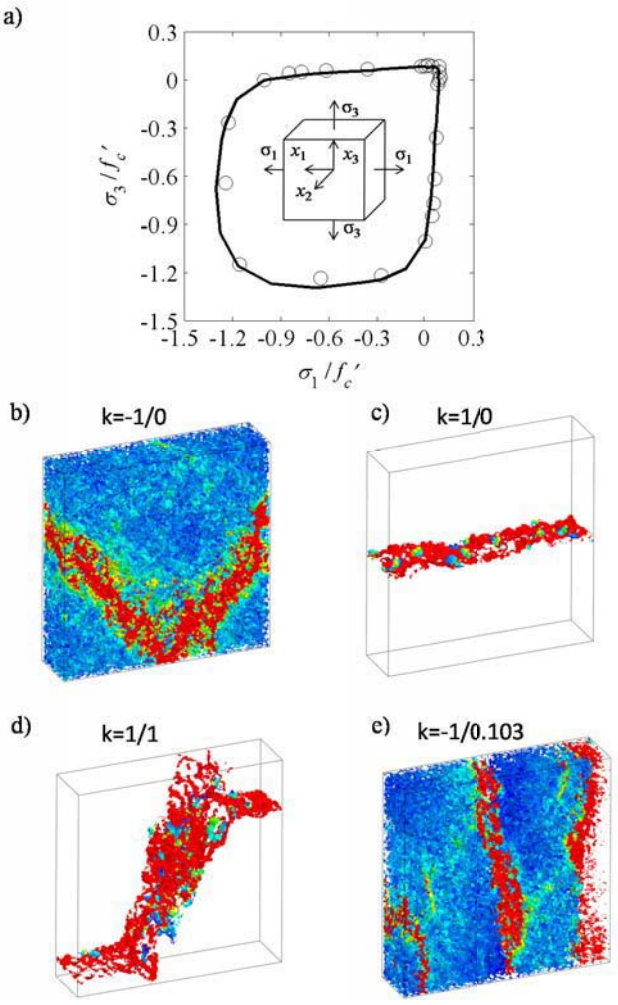

Figure 4: Biaxial test results.

compressive strength. The numerical results fit the experimental data very well. Both the experiments and the numerical simulations show that compressive concrete strength increases as a function of k and reaches its maximum for $k \approx 0.5$.

It is interesting to analyze the failure modes under some characteristic loading paths. In Figure 4b, one can see the failure mode (identified through contours of mesoscale crack openings) associated with uniaxial compression (k =-1/0). The numerical simulation predicts the classical shear bands with an inclination of about 45 degrees. Failure under uniaxial tension (k ==1/0), featuring one localized crack orthogonal to the direction of loading, is reported in Figure 4c. Figure 4d shows the fracture path associated with equibiaxial tension (k =1/1). Under this load condition, the specimen fails with an inclined fracture of about 45 degrees. Finally, Figure 4e reports the failure mode associated with compression and transverse tension (k =-1/0.103). Although the transverse tension is about one tenth of the compression, its presence is sufficient to change the failure mode from a shear band (observed for pure compression) to a splitting crack.

5 TRIAXIAL COMPRESSION

Concrete strength and ductility depend strongly on the degree of confinement. Under multiaxial stress states, mesoscale tensile fracturing and shearing are prevented, making strain softening reverse into strain hardening. LDPM simulations of triaxial tests are reported herein. The simulated experimental data are relevant to experiments performed at Engineer Research Development Center (ERDC) and are already published in Caner et al. (2000). In these experiments, 76.2 mm $\times$ 152.4 mm cylindrical specimens were first submitted to a hydrostatic pressure up to a desired confinement value (Fig. 5c). Later, while the transverse confinement was kept constant, the longitudinal stress was continuously increased up to either failure or a maximum longitudinal strain of 10 %. Confining pressures from 20 MPa up to 600 MPa were considered.

Figure 5a reports the comparison between the numerical simulations (solid curves) and the experimental results (circles). The agreement is excellent, and both the experimental and the numerical results show significant strength increase as a function of the confining pressure. For a confining pressure of 600 MPa, the strength is more than 25 times the unconfined uniaxial strength. In addition, at high confining pressures the behavior is very ductile and longitudinal strains up to 10 % are reached without reduction of the load carrying capacity. Figure 5d shows the simulated failure mode during triaxial tests. The failure, as typically reported in the experiments, is associated with the formation of an inclined shear band.

Figure 5b shows the comparison between the experimental data and the hydrostatic test and uniaxial

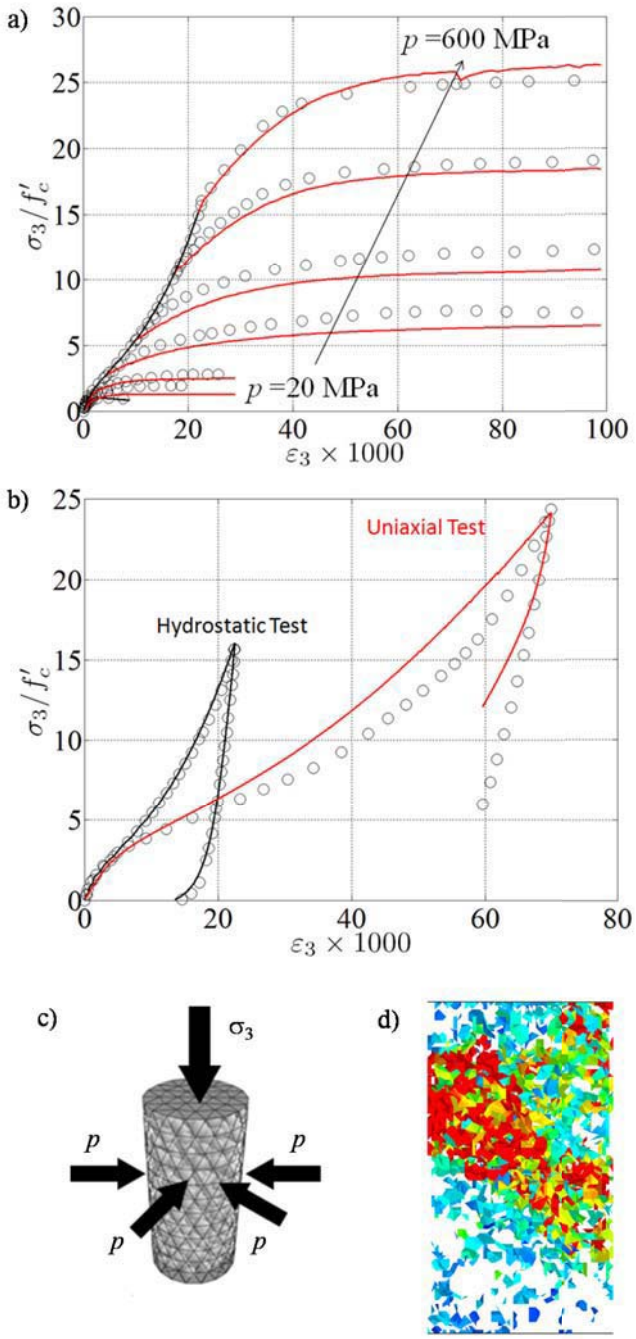

Figure 5: Triaxial test results.

strain test data. The latter test is conducted by fully restraining the transverse expansion of the specimens while loaded longitudinally. As one can see, LDPM is able to reproduce very well the experimental evidences in both tests in both the loading and unloading phases. In particular, LDPM succeeds in predicting the more compliant behavior during the uniaxial strain test. This result is particularly noteworthy since most continuum-based models currently available for the simulation of concrete do not perform well under this loading condition and since they can be calibrated to fit either the hydrostatic curve or the uniaxial strain curve, but not both.

6 FIBER REINFORCED CONCRETE

Recently, LDPM has been extended to include the effect of randomly dispersed fibers. During the pre-processing phase, each individual fiber is inserted in the specimen volume. Fiber positions and orientations are randomly generated, and the intersection between each fiber and the LDPM facets are detected. Stresses on each LDPM facets can be computed as

$$\boldsymbol{\sigma} = \boldsymbol{\sigma}_c + \frac{1}{A_c} \sum_{f \in A_c} \mathbf{F}_f(\mathbf{w}, d_f, L_{sf}, L_{lf}, \mathbf{n}_f) \qquad (13)$$

where $\boldsymbol{\sigma} = [\sigma_N \ \sigma_M \ \sigma_L]^{\mathrm{T}}$, $\boldsymbol{\sigma}_c = [\sigma_{Nc} \ \sigma_{Mc} \ \sigma_{Lc}]^{\mathrm{T}}$, and $\mathbf{F}_f = [F_{Nf} \ F_{Mf} \ F_{Lf}]^{\mathrm{T}}$ represents the fiber contribution. The concrete stress components σ_{Nc}, σ_{Mc}, and σ_{Lc} are computed according to the LDPM constitutive law presented in Section 1. The fiber contribution, $\mathbf{F}_f$, is computed according to the micro-structural fiber-matrix interaction model developed by Lin and coworkers (Lin et al. 1999), and it depends on facet crack opening, $\mathbf{w}$; fiber geometry (d_f = fiber diameter, L_{sf} = short embedment length, L_{lf} = long embedment length); and fiber orientation with to respect to the crack (facet) plane, $\mathbf{n}_f$). Equation 13 is consistent with the assumption of a parallel coupling at facet level between concrete matrix and fibers.

Simulation of the fiber effect on the tensile fracturing behavior of concrete is shown in Figure 6. The experimental data are relevant to experiments reported by Li et al. (1998). In this experimental investigation, dog-bone shaped specimens were subjected to direct tension. The tests were controlled through displacement measurements over a measure length of 120 mm to ensure the stability in the post-peak and softening regime. The simulated fibers were Dramix steel fibers with hooked ends characterized by a diameter of 0.5 mm and a length of 30.0 mm.

Figure 6a shows experimental and numerical stress versus displacement curves for three different fiber volume fractions, 0% (plain concrete), 2%, and 6%. LDPM is able to predict the increased strength and ductility due to the effect of fibers. The behavior gradually transitions from softening for plain concrete and low fiber volume fractions to hardening for high fiber volume fractions.

LDPM numerical results are further investigated in Figure 6b, where contours of the meso-scale crack-opening at the end of the simulations are reported for the various fiber volume fractions. For plain concrete, the crack pattern is characterized by one localized crack that propagates from one side towards the other side of the specimen. As fracture propagates, material outside the crack unloads as the overall load applied to the specimen tends to zero. For the 2% volume fraction, one main crack propagates, but the entire specimen features diffuse cracking, and no unloading occurs. Absence of unloading outside the main crack is attributed to the fact that, even though the overall behavior is still softening, the stress versus displacement curve shows a non-zero residual stress associated with the fiber crack bridging effect. Finally, for the 6% volume fraction, the crack pattern is characterized by several branched cracks whose propagation is arrested by the effect of the fibers. No unloading occurs outside the main cracks, since the overall behavior is strain-hardening and, up to a displacement of 0.5 mm (average nominal strain of 0.5 mm / 120 mm $\approx$ 0.42%), no reduction of the load carrying can be observed.

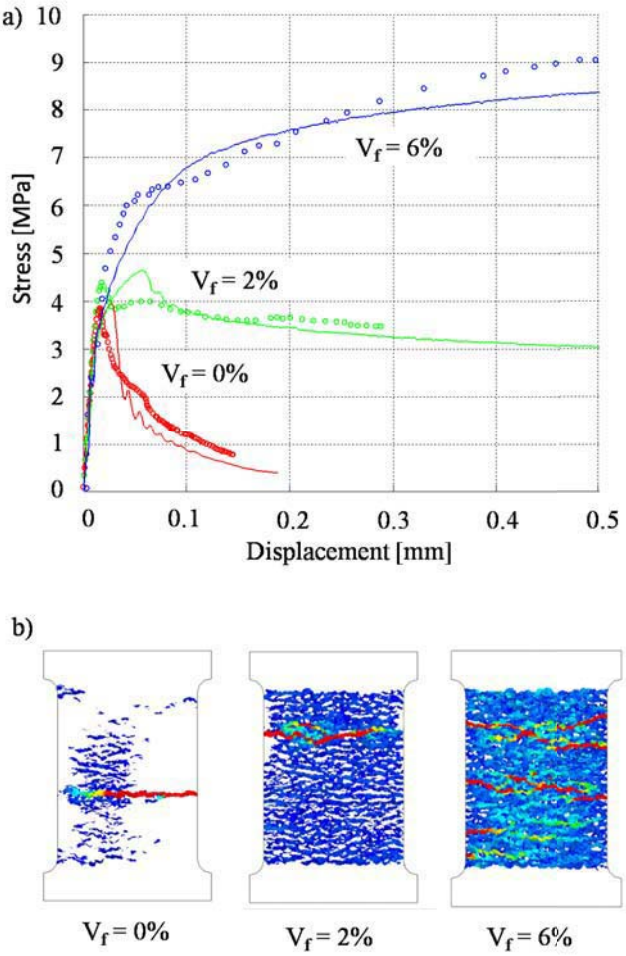

Figure 6: Simulation of fiber reinforced concrete.

7 CONCLUSION

This paper presents recent results obtained through the Lattice Discrete Particle Model (LDPM). LDPM shows unprecedented predictive capabilities under an extremely wide variety of conditions, including tensile fracture, uniaxial compression, biaxial tension and compression, and triaxial compression. The unique feature of LDPM, enabled by its meso-scale character, is its ability to simulate softening macroscopic behavior in compression as a result of meso-scale tensile fracture and shearing without the need of a phenomenologically formulated compressive softening. This, in turn, allows automatically the simulation of the transition from strain softening to strain hardening due to confining effects.

In addition, the meso-scale formulation of LDPM provides an ideal framework for the simulation of

fiber effects and, consequently, for the modeling of fiber reinforced concrete (FRC). Preliminary results relevant to the tensile behavior of FRC with steel fibers demonstrate LDPM's capability of predicting the increase of strength and ductility as function of fiber volume fraction.

8 ACKNOWLEDGMENT

This effort was sponsored by the U.S. Army Engineer Research and Development Center (ERDC). Permission to publish was granted by the Director, Geotechnical and Structures Laboratory, ERDC.

REFERENCES

Bažant, Z.P., and Oh, B.H., 1983. Crack band theory for fracture of concrete. *Mater. Structures, RILEM* 16: 155-177.

Bažant, Z.P., Tabbara, M.R., Kazemi, T., and Pijaudier-Cabot, G., 1990. Random particle model for fracture of aggregate or fiber composites. *J. Eng. Mech.* 116(8): 1686-1705.

Bažant, Z.P., Planas, J., *Fracture and size effect in concrete and other quasibrittle materials*, Boca Raton and London, CRC Press, 1998.

Caner, F.C., and Bažant, Z.P., 2000. Microplane model M4 for concrete. II: Algorithm and calibration. *J. of Engrg. Mechanics, Trans. ASCE* 126(9): 954-961.

Carol, I., López, C.M., and Roa, O., 2001. Micromechanical analysis of quasi-brittle materials using fracture-based interface elements. Internat. *J. Numer. Methods Engrg.* 52: 193-215.

Cusatis, G., Bažant, Z.P., and Cedolin, L., 2003. Confinement-shear lattice model for concrete damage in tension and compression: I. Theory. *J. of Engrg. Mech. (ASCE)* 129(12): 1439-1448.

Cusatis, G., Bažant, Z.P., and Cedolin, L., 2003. Confinement-shear lattice model for concrete damage in tension and compression: II. Computation and validation. *J. of Engrg. Mech. (ASCE)* 129(12): 1449-1458.

Cusatis, G., Bažant, Z.P., and Cedolin, L., 2006a. Confinement-shear lattice model for fracture propagation in concrete. *Comput. Methods Appl. Mech. Engrg.* 195: 7154-7171.

Cusatis, G., Cedolin, L., 2006b. Two-scale analysis of concrete fracturing behavior. *Engng. Fracture Mech.* 74: 317.

Kupfer, H., Hilsdorf, H.K., and Rusch, H., 1969. Behavior of concrete under biaxial stresses. *J. Am. Concrete. Inst.* 66(8): 656-666.

Li, Z., Li, F., Chang, T.-Y.P., and Mai, Y.-W., 1998. Uniaxial tensile behavior of concrete reinforced with randomly distributed short fibers. *ACI Material Journal.* October, 564-574.

Lilliu, G., and Van Mier, J.G.M., 2003. 3D lattice type fracture model for concrete. *Engng. Fracture Mech.* 70: 927-941.

Lin, Z., Kanda, T., and Li, V.C., 1999. On interface characterization and performance of fiber-reinforced cementitious composites. *Concr. Sc. Engng.* 1: 173-184.

Pelessone, D., 2009. MARS, Modeling and Analysis of the Response of Structures - User's Manual, ES3, Solana Beach (CA), USA. http://www.es3inc.com/mechanics/MARS/Online/MarsManual.htm.

Roelfstra, P.E., Sadouki, H., and Wittmann, F.H., 1985. Le béton numérique. *Mater. Struct.* 18: 327-335.

Schlangen, E., and Van Mier, J.G.M., 1992. Shear fracture in cementitious composites, Part II: Numerical simulations. *Fracture mechanics of concrete structures, Proc. FraMCoS-1*, Bažant Z. P., London, Elsevier, 671-676.

Van Mier, J.G.M., Shah, S.P., Arnaud, M., Balayssac, J.P., Bascoul, A., Choi, S., Dasenbrock, D., Ferrara, G., French, C., Gobbi, M.E., Karihaloo, B.L., Konig, G., Katsovos, M.D., Labuz, J., Lange-Kornbak, D., Markeset, G., Pavlovic, M.N., Simsch, G., Thienel, K.C., Turatsinze, A., Ulmer, M., Van Geel, H., J.G.M. and Van Vliet, M.R.A., and Zissopoulos, D., 1997. Strain-softening of concrete in uniaxial compression - Report of the Round Robin Test carried out by RILEM TC 148-SSC. *Materials and Structures.* 198(30):195-209.

Van Mier, J.G.M., Vervuurt, A., and Schlangen, E., 1994. Boundary and size effects in uniaxial tensile tests: A numerical and experimental study. *Fracture and damage in quasibrittle structures, Proc. NSF Workshop.* Prague, Bažant Z. P., Bittnar, Z., Jirásek, M., Mazars, J., London, E & FN Spon, 289-302.

Wittmann, F.H., Roelfstra, P.E., and Kamp, C.L., 1988. Drying of concrete: an application of the 3L-approach. *Nucl. Eng. Des.* 105: 185-198.

Yip, M., Li, Z., Liao, B.-S., and Bolander, J.E., 2006. Irregular lattice models of fracture of multiphase particulate materials. *International J of Fracture* 140(1-4): 113-124.